

Statistical Comparison of Dynamic Contrast-Enhanced MRI Pharmacokinetic Models in Human Breast Cancer

Xia Li,^{1,2} E. Brian Welch,^{1,2} A. Bapsi Chakravarthy,^{3,11} Lei Xu,⁴ Lori R. Arlinghaus,^{1,2} Jaime Farley,¹¹ Ingrid A. Mayer,⁶ Mark C. Kelley,^{7,11} Ingrid M. Meszoely,^{7,11} Julie Means-Powell,^{6,11} Vandana G. Abramson,^{6,11} Ana M. Grau,^{7,11} John C. Gore,^{1,2,5,8,9,11} and Thomas E. Yankeelov^{1,2,5,8,10,11*}

By fitting dynamic contrast-enhanced MRI data to an appropriate pharmacokinetic model, quantitative physiological parameters can be estimated. In this study, we compare four different models by applying four statistical measures to assess their ability to describe dynamic contrast-enhanced MRI data obtained in 28 human breast cancer patient sets: the chi-square test (χ^2), Durbin–Watson statistic, Akaike information criterion, and Bayesian information criterion. The pharmacokinetic models include the fast exchange limit model with (FXL_{v_p}) and without (FXL) a plasma component, and the fast and slow exchange regime models (FXR and SXR, respectively). The results show that the FXL_{v_p} and FXR models yielded the smallest χ^2 in 45.64 and 47.53% of the voxels, respectively; they also had the smallest number of voxels showing serial correlation with 0.71 and 2.33%, respectively. The Akaike information criterion indicated that the FXL_{v_p} and FXR models were preferred in 42.84 and 46.59% of the voxels, respectively. The Bayesian information criterion also indicated the FXL_{v_p} and FXR models were preferred in 39.39 and 45.25% of the voxels, respectively. Thus, these four metrics indicate that the FXL_{v_p} and the FXR models provide the most

complete statistical description of dynamic contrast-enhanced MRI time courses for the patients selected in this study. *Magn Reson Med* 68:261–271, 2012. ©2011 Wiley Periodicals, Inc.

Key words: DCE-MRI; water exchange; breast cancer; pharmacokinetic modeling

Dynamic contrast-enhanced MRI (DCE-MRI) involves the acquisition of images before and after an intravenous injection of contrast agent (CA). By fitting DCE-MRI data to a pharmacokinetic model, quantitative physiological parameters such as the volume transfer constant (K^{trans}), extravascular-extracellular volume fraction (v_e), and the plasma fraction (v_p) can be estimated (1–3). In diagnosing breast cancer, DCE-MRI has shown high sensitivity (77–100%) but moderate specificity (26–97%) ((4–8), reviewed in Ref. 9). In monitoring treatment response in breast cancer, there have been many efforts using DCE-MRI as a surrogate biomarker for predicting response to neoadjuvant chemotherapy. Several investigators have proposed both semiquantitative and quantitative methods for classifying contrast enhancement curves and have used this information to delineate complete response from partial response and progressive disease (see, e.g., Refs. 10–20). For example, some investigators have shown that changes in tumor size as measured by dynamic MRI significantly correlate with residual disease at time of surgery (e.g., Refs. 10–13). Considering the potentially more difficult question of predicting treatment response early in the course of therapy, some investigators have shown that changes in tumor volume as measured by dynamic MRI after one cycle of therapy significantly correlate with pathologic response (e.g., Refs. 14 and 15). Morphological characteristics (such as tumor size) are the downstream effects of underlying physiological changes, so it seems reasonable that changes in metrics of tumor perfusion could serve as biomarkers of early response to treatment.

However, the literature presents differing results regarding the predictive value of quantitative modeling of DCE-MRI data; some have shown that kinetic analysis was not predictive after early therapy (15,21), whereas others have shown that it is (14,22). These contradictory results may not be surprising considering the significant differences in tumor type, treatment regimen, number of patients, clinical and pathological endpoints, imaging data acquisition, and data analysis techniques. Another possible reason for such apparent discrepancies is that the standard DCE-MRI model used to analyze such data may not adequately describe the relevant physiology.

¹Institute of Imaging Science, Vanderbilt University, Nashville, Tennessee, USA.

²Department of Radiology and Radiological Sciences, Vanderbilt University, Nashville, Tennessee, USA.

³Department of Radiation Oncology, Vanderbilt University, Nashville, Tennessee, USA.

⁴Department of Biostatistics, Vanderbilt University, Nashville, Tennessee, USA.

⁵Department of Biomedical Engineering, Vanderbilt University, Nashville, Tennessee, USA.

⁶Department of Medical Oncology, Vanderbilt University, Nashville, Tennessee, USA.

⁷Department of Surgical Oncology, Vanderbilt University, Nashville, Tennessee, USA.

⁸Department of Physics and Astronomy, Vanderbilt University, Nashville, Tennessee, USA.

⁹Department of Molecular Physiology and Biophysics, Vanderbilt University, Nashville, Tennessee, USA.

¹⁰Department of Cancer Biology, Vanderbilt University, Nashville, Tennessee, USA.

¹¹Vanderbilt Ingram Cancer Center, Vanderbilt University, Nashville, Tennessee, USA.

Grant sponsor: National Institutes of Health; Grant numbers: NCI 1R01CA129961, NCI 1P50 098131, and NCI 1U01CA142565; Grant sponsor: Vanderbilt-Ingram Cancer Center; Grant number: NIH P30 CA68485

*Correspondence to: Thomas E. Yankeelov, Ph.D., Vanderbilt University Medical Center, Institute of Imaging Science, Vanderbilt University, AA-1105 Medical Center North, 1161 21st Avenue South, Nashville, TN 37232-2310. E-mail: thomas.yankeelov@vanderbilt.edu

Received 14 April 2011; revised 9 August 2011; accepted 14 August 2011.

DOI 10.1002/mrm.23205

Published online 29 November 2011 in Wiley Online Library (wileyonlinelibrary.com).

The standard model relies on a linear dependence between the measured longitudinal relaxation rate constant R_1 ($\equiv 1/T_1$) and the concentration of CA in tissue (23,24). This model assumes that tissue is effectively one well-mixed compartment of water; in MRI, this assumption is referred to as the fast exchange limit (FXL). Several studies have presented evidence that this assumption is violated in vivo especially when the concentration of CA in the voxel of interest is high, and efforts have been made to develop analyses that do not make this assumption (23–29). By considering the extravascular space as two separate compartments, an extravascular-extracellular space and an extravascular-intracellular space, models can be built that account for the limited rate of water exchange between these compartments. This “fast exchange regime” (FXR) model has revealed that significant errors may arise when using the FXL analysis (24). In particular, initial applications of the FXR model to human breast cancer DCE-MRI data suggest that the FXL formalism used in these studies can grossly underestimate blood flow, vessel wall permeability, and extravascular-extracellular volume fractions (27–29).

Although a few of studies have performed comparisons of kinetic models for DCE-MRI data of the prostate or cervix (30,31), none has been performed for breast cancer. Here, we report the results of standard statistical tests on the breast cancer DCE-MRI analyses provided by the FXL with and without a vascular term and the fast and slow exchange regime models (FXR and SXR, respectively) to assess which model is most robust in a statistical sense. Because DCE-MRI ultimately aims to positively impact clinical diagnosis and prediction of treatment response, the choice of model to perform the analysis is of central importance.

MATERIALS AND METHODS

Data Acquisition

Fifteen patients with locally advanced breast cancer were enrolled in an ongoing clinical trial (32). The patients provided informed consent, and the study was approved by the ethics committee of the Vanderbilt-Ingram Cancer Center. DCE-MRI was performed using a Philips 3T Achieva MR scanner (Philips Healthcare, Best, The Netherlands). A four-channel receive double-breast coil covering both breasts was used for all imaging (Invivo Inc., Gainesville, FL). Data for constructing a T_1 map were acquired with an radiofrequency-spoiled three-dimensional gradient echo multiframe approach with TR = 7.9 ms, TE = 1.3 ms, and 10 flip angles from 2° to 20° in 2° increments. The acquisition matrix was 192 × 192 × 20 (full-breast) over a sagittal square field of view (22 cm²) with slice thickness of 5 mm, one signal acquisition, and a sensitivity encoding (SENSE) factor of 2 for an acquisition time of just under 3 min. The dynamic scans used identical parameters and a flip angle of 20°. Each 20-slice set was collected in 16 s at 25 time points for ~7 min of scanning. A catheter placed within an antecubital vein delivered 0.1 mmol/kg (9–15 mL) of the CA gadopentetate dimeglumine, Gd-diethylenetriamine penta-acetic acid (DTPA) (Magnevist, Wayne, NJ) at 2 mL/s (followed by a saline flush) via a power injector after the acquisition

of three baseline dynamic scans for the DCE study. Four patients were scanned at three time points: pretreatment, after one cycle of neoadjuvant chemotherapy, and after all cycles of chemotherapy; and the other 11 patients were scanned at the first two time points, yielding a total of 34 data sets. Six out of the 34 data sets failed to characterize the first pass or wash-out features of the arterial input function (AIF), yielding a total of 28 useable data sets.

Theory

The measured signal intensity from a spoiled gradient echo acquisition can be described by Eq. 1:

$$S(t) = S_0 \sin \alpha \frac{1 - \exp(-TR/T_1(t))}{1 - \cos \alpha \exp(-TR/T_1(t))}, \quad [1]$$

where α is the flip angle, TR is the repetition time of the excitation radiofrequency pulse of the MR imaging sequence, S_0 is a constant describing the scanner gain and proton density, and we have assumed that $TE \ll T_2^*$. To perform quantitative DCE-MRI data analysis, the time-varying longitudinal relaxation time, $T_1(t)$, must be related to the concentration of CA in the tissue, $C_t(t)$. Usually, a linear relationship between the two quantities is assumed:

$$R_1(t) \equiv 1/T_1(t) = r_1 C_t(t) + R_{10}, \quad [2]$$

where R_{10} is the R_1 value of the tissue before CA administration and r_1 is the relaxivity of the CA. In actual DCE-MRI experiments, the C_t time course cannot be directly measured, and thus Eq. 2 needs to be expressed in terms of the quantities that are actually measurable in an MRI experiment (i.e., the relaxation rate constants). Toward this end, we use the Kety relationship (33):

$$C_t = K^{\text{trans}} \cdot \int_0^T C_p(t) \cdot e^{-(K^{\text{trans}}/v_e) \cdot (T-t)} dt, \quad [3]$$

where K^{trans} is the CA extravasation rate constant, v_e is the extravascular-extracellular volume fraction, and $C_p(t)$ is the concentration of CA in blood plasma, also known as the AIF. In this study, a semiautomatic AIF tracking algorithm is used to calculate the AIF for each patient. This algorithm is initialized by defining a kernel centered on a manually selected seed point within the axillary artery in one slice. In an adjacent slice, the center of the artery is detected through searching the maximum Pearson correlation coefficient (CC) of the signal intensity between the kernel and the region of interests in the adjacent slice. The procedure is repeated for all slices to find all voxels within the artery that are then used to construct an AIF; more details are provided in Ref. 34.

A more complex model incorporates the blood plasma volume fraction, v_p :

$$C_t(T) = K^{\text{trans}} \int_0^T C_p(t) \exp(-(K^{\text{trans}}/v_e)(T-t)) dt + v_p C_p(t). \quad [4]$$

Substituting Eqs. 3 and 4 into 2 yields Eqs. 5 and 6, respectively:

$$R_1(t) = r_1 K^{\text{trans}} \cdot \int_0^T C_p(t) \cdot e^{-(K^{\text{trans}}/v_e) \cdot (T-t)} dt + R_{10}, \quad [5]$$

$$R_1(t) = r_1 K^{\text{trans}} \cdot \int_0^T C_p(t) \cdot e^{-(K^{\text{trans}}/v_e) \cdot (T-t)} dt + r_1 v_p C_p(t) + R_{10}. \quad [6]$$

Equations 5 and 6 are two of four models we assess in the study, which are termed the FXL and FXL_{v_p}, respectively.

The “fast exchange” limit relationship described above is equivalent to assuming that all water compartments within the tissue are well mixed so the effects of the CA are completely described by a single rate constant. However, tissue is not homogeneous, but rather it may be compartmentalized within an MRI voxel. The use of Eq. 2 for the entire ¹H₂O signal from a voxel requires that water exchange between the vascular, extravascular-intracellular space, and the extravascular-extracellular spaces are sufficiently fast. In practice, this is often not the case; and, when it is not, the Bloch equations should incorporate the effects of this exchange, leading to longitudinal relaxation that can be characterized by biexponential decay:

$$S(t) = a_L S_{0L} \sin \alpha \frac{1 - \exp(-TR/T_{1L}(t))}{1 - \cos \alpha \exp(-TR/T_{1L}(t))} + a_S S_{0S} \sin \alpha \frac{1 - \exp(-TR/T_{1S}(t))}{1 - \cos \alpha \exp(-TR/T_{1S}(t))}, \quad [7]$$

where

$$a_L = \frac{f_w / (v_e \tau_i)}{\left(\left(\frac{2}{\tau_i} - \frac{f_w}{v_e \tau_i} \right)^2 + \left(\frac{4}{\tau_i^2} \left(\frac{f_w}{v_e} - 1 \right) \right) \right)^{1/2}}, \text{ and } a_S = \frac{1}{2} - \frac{1}{2} a_L, \quad [8]$$

and

$$R_{1S,1L}(t) = 1/T_{1S,1L} = \frac{1}{2} \left(2R_{1i} + r_1 C_t(t) + \frac{(R_{10} - R_{1i} + 1/\tau_i)}{(v_e/f_w)} \right) \pm \frac{1}{2} \left(\left(\frac{2}{\tau_i} - r_1 C_t(t) - \frac{R_{10} - R_{1i} + 1/\tau_i}{v_e f_w} \right)^2 + 4 \frac{(1 - v_e/f_w)}{\tau_i^2 (v_e/f_w)} \right)^{1/2}. \quad [9]$$

T_{1S} and T_{1L} are the apparent shorter and longer T_1 components, respectively, R_{1i} is the intracellular R_1 , τ_i is the average intracellular water lifetime of a water molecule, and f_w is the fraction of water that is accessible to mobile CA (23–25), which is set to 1.0 in this study. Equation 9 with and without the T_{1S} yields the other two models that we evaluate, which are termed the FXR and SXR models, respectively (24).

Statistical Analysis

We used four common statistical tests to assess the analyses provided by Eqs. 5, 6, and 9. The first is the Durbin–Watson (D–W) statistic that is a commonly used test

for detecting serial correlation in residuals (35) and is computed via Eq. 10:

$$d = \frac{\sum_{i=1}^n (e_i - e_{i-1})^2}{\sum_{i=1}^n e_i^2} \quad [10]$$

where e_i are the residuals. In regression analysis, errors are typically assumed to be pairwise uncorrelated; serial correlation is a special case in which correlations between errors separated by i steps are similar (35). If residuals exhibit positive serial correlation, successive residuals tend to be similar, whereas in negative serial correlation, the successive residuals are dissimilar. Equation 10 provides a way of quantifying these phenomena. When the D–W statistic shows significant serial correlation, the fitting model should be questioned. The range of d lies between 0 and 4; but to establish the significance of d values upper and lower bounds (d_U and d_L , respectively) must be evaluated. Those bounds are determined by the number of observations, the number of free parameters in the model, and the desired significance threshold. If $d < d_L$ or $4-d < d_L$, then d is considered significant for either positive or negative serial correlation, respectively. If $d_L < d < d_U$, then the D–W statistic is indeterminate.

The second statistical test applied to the models is the standard chi-square test, χ^2 , which is given as Eq. 11:

$$\chi^2 = \sum_{i=1}^n \frac{(y_{\text{fit}} - y_i)^2}{n_o}, \quad [11]$$

where y_{fit} is the estimated value of the actual data, y_i , and n_o is the number of degrees of freedom.

The third statistical test used to determine the validity of the models is the Akaike information criterion (AIC). Given a set of models, the AIC is a method to select the model that best balances goodness of fit with number of free parameters (36). It is computed via Eq. 12:

$$\text{AIC}_c = 2k + n \ln \left(\frac{\text{RSS}}{n} \right) + \frac{2k(k+1)}{n-k-1}, \quad [12]$$

where n is the number of observations, k is the number of parameters, and RSS is the residual sum of squares. Note that Eq. 12 is the form of the AIC that includes a second-order correction to account for a small number of observations; this is typically denoted by the subscript “c” on “AIC.” In the experimental data presented below, there are 25 observations in the DCE time series data and the FXL model has two free parameters, whereas the FXL_{v_p}, FXR, and SXR models each have three free parameters. The model returning the lowest AIC_c value is the model that represents the best balance between complexity (i.e., the number of free parameters) and goodness of fit (i.e., lower RSS).

The fourth and final statistical test we used is the Bayesian information criterion (BIC), which is also used to detect the balance between the goodness of fit and the model complexity. AIC_c and BIC measure a model similarly, except that the BIC applies a heavier penalty on the model complexity:

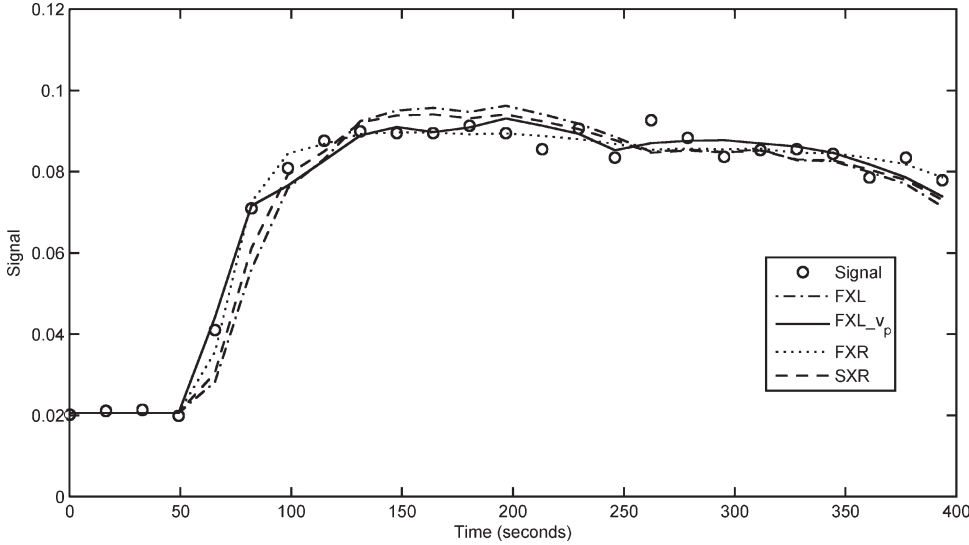


FIG. 1. An example of the plots of the fit and experimental data. Please note that the “waviness” in the fit curve is due to the noise in the individually measured AIF; when the AIF is smoothed, the waviness is eliminated.

$$\text{BIC} = n \ln\left(\frac{\text{RSS}}{n}\right) + k \ln(n). \quad [13]$$

Data Analysis

Precontrast T_1 values, T_{10} values were computed by fitting the multiflip angle data to Eq. 1. Voxels for which Eq. 1 could not fit the data were set to zero and not included in the analysis. Data from each DCE-MRI study were fit on a voxel-by-voxel basis with Eqs. 5, 6, and 9 to yield estimates of K^{trans} (all models), v_e (all models), v_p (FXL_ v_p model only), and τ_i (FXR and SXR only). The fitting routine uses a standard gradient-expansion, non-linear, least-square, curve-fitting algorithm written in the Interactive Data Language (RSI, Boulder, CO).

Implicit in this analysis is the requirement for measuring or estimating the AIF. We have proposed a simple and efficient method (34) to obtain the AIF, through tracking an initial seed point placed within the axillary artery. Using this method, we obtain the AIF for each individual patient. Voxels for which the fitting algorithm did not converge, or converged to unphysical values (e.g., $K^{\text{trans}} > 5.0 \text{ min}^{-1}$, $v_e > 1$, $v_p > 1$, $\tau_i > 3.0 \text{ s}$, or any parameter below zero) were set equal to zero. Along with the parameter estimates, values for D-W, χ^2 , AIC_c, and BIC statistics were also saved for each voxel. Voxels were defined as “enhancing” if the averaged postcontrast

signal intensities increased by 50% over the average signal intensity precontrast time points.

RESULTS

Figure 1 shows an example of the model fit to the experimental data for one enhancing tumor pixel. For this data, the mean absolute differences between the experimental data and the fit data returned by FXL, FXL with v_p , FXR, and SXR are 0.0044, 0.0022, 0.0019, and 0.0034, respectively. (Please note that the “waviness” in the fit curve is due to the noise present in the individually measured AIF; that is, a smoothed AIF would result in a smoothed fit.)

Figure 2 shows an example of K^{trans} parametric maps returned by the four models; from left to right, the maps were obtained from the FXL, FXL_ v_p , FXR, and SXR, respectively. The AIF obtained from this patient by our method (34) is also shown in the figure. Observe how the SXR model cannot estimate the K^{trans} values for most of the tumor voxels; the SXR model could converge on only $35 \pm 15\%$ of the enhancing tumor voxels, whereas the FXL, FXL_ v_p , and FXR models can converge on 74 ± 17 , 56 ± 16 , and $72 \pm 16\%$ of the enhancing voxels, respectively. As we need to compare all models involved for each voxel, if we examine the voxels only for which the SXR returns an accurate fit, this greatly reduces the number of data points available for comparison. For this reason, we did

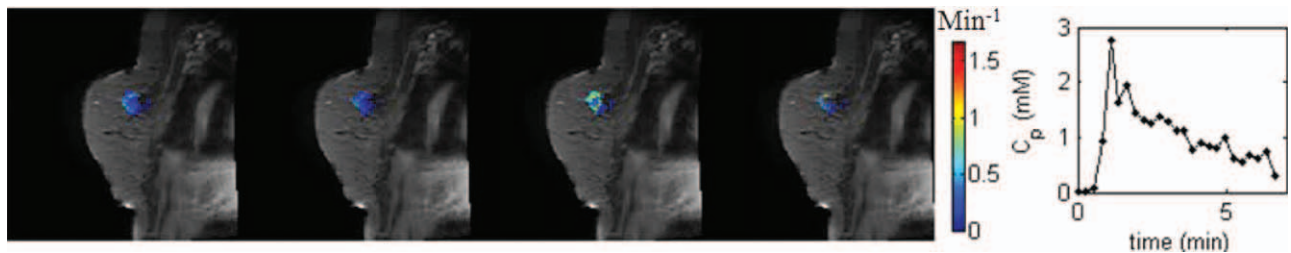


FIG. 2. An example of the K^{trans} values returned by the four models; from left to right, the maps are given by FXL, FXL_ v_p , FXR, and SXR models. The AIF obtained from this patient (by our previously proposed method) is also shown on the right. It is clear that model selection can greatly affect the parameter values that are returned, and this is why it is necessary to develop a method to select which model is most appropriate.

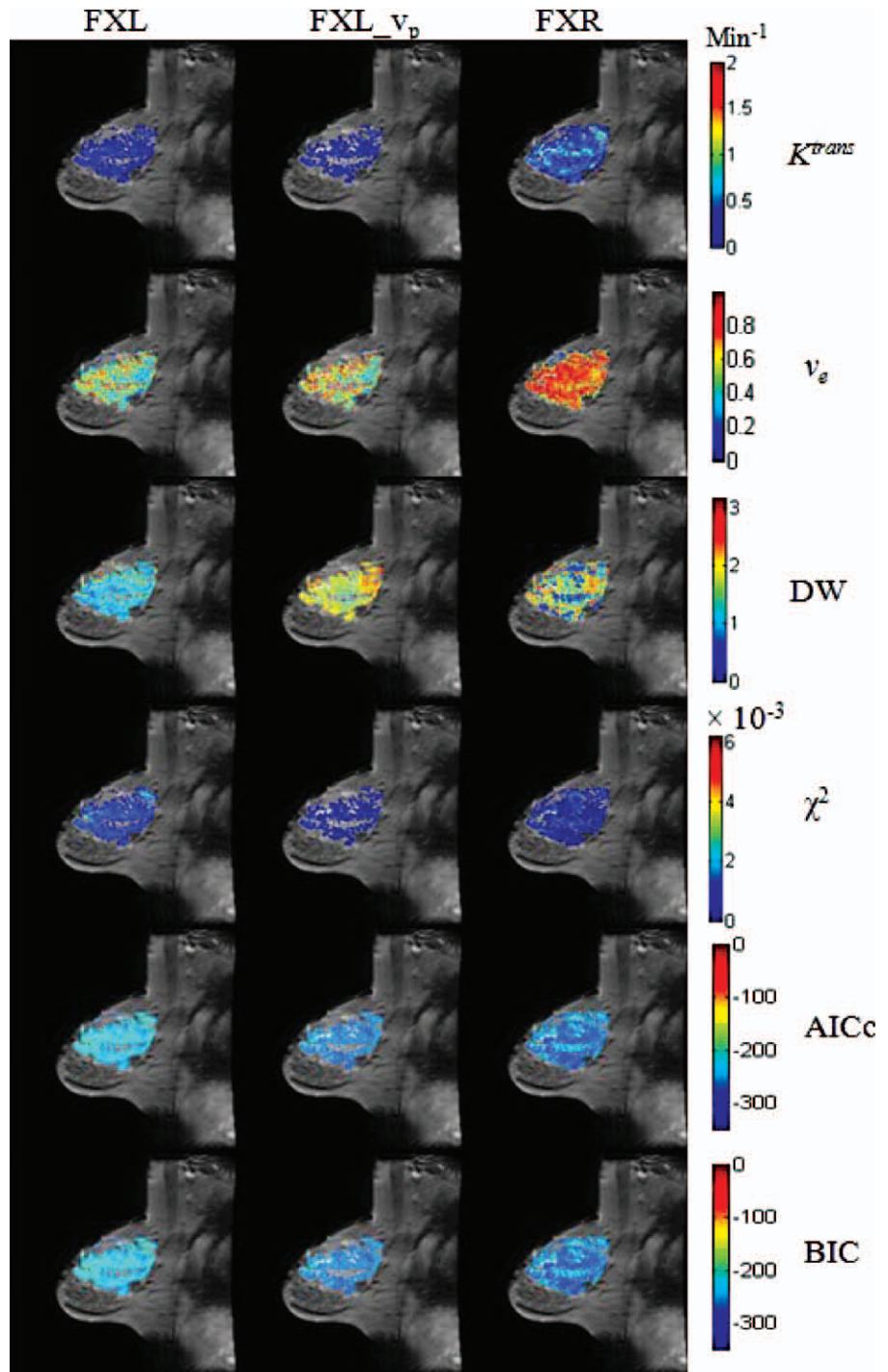


FIG. 3. An example of the K^{trans} , v_e , D-W, χ^2 , AIC_c, and BIC parametric maps superimposed on the central tumor slice of one patient. These maps were obtained by FXL (left column), FXL_{vp} (middle column), and FXR (right column), respectively. In the majority voxels displaying contrast enhancement, the χ^2 , AIC_c, and BIC all prefer the FXL_{vp} and FXR analyses.

not continue the analysis with the SXR model; and hereafter, we focus on the remaining three models. We return to this point in the “Discussion” section.

Figure 3 shows an example in which the parametric maps of K^{trans} , v_e , D-W, χ^2 , AIC_c, and BIC are superimposed on a postcontrast, central slice through the tumor of one patient. The maps were obtained from fitting the signal intensity time courses by the FXL (left column), FXL_{vp} (middle column), and FXR (right column), respectively. For this specific case, the FXL led to the smallest mean D-W value. The χ^2 , AIC_c, and BIC all favor the FXR analysis in ~92% of the enhancing voxels.

Figure 4 displays the box and whisker plots of K^{trans} values obtained by the FXL, FXL_{vp}, and FXR models for each data set. The figure shows a clear trend that FXL_{vp} leads to the smallest median K^{trans} values, whereas the FXR model results in the largest median K^{trans} values in ~90% of the data sets. This phenomenon is consistent with the physical assumptions of the FXL_{vp} model, as it includes a term for the vascular volume, which results in reduced vessel perfusion and permeability values. Similarly, the v_e values obtained by the three models for each data set are displayed in Fig. 5. This figure shows the FXR led to the largest median v_e

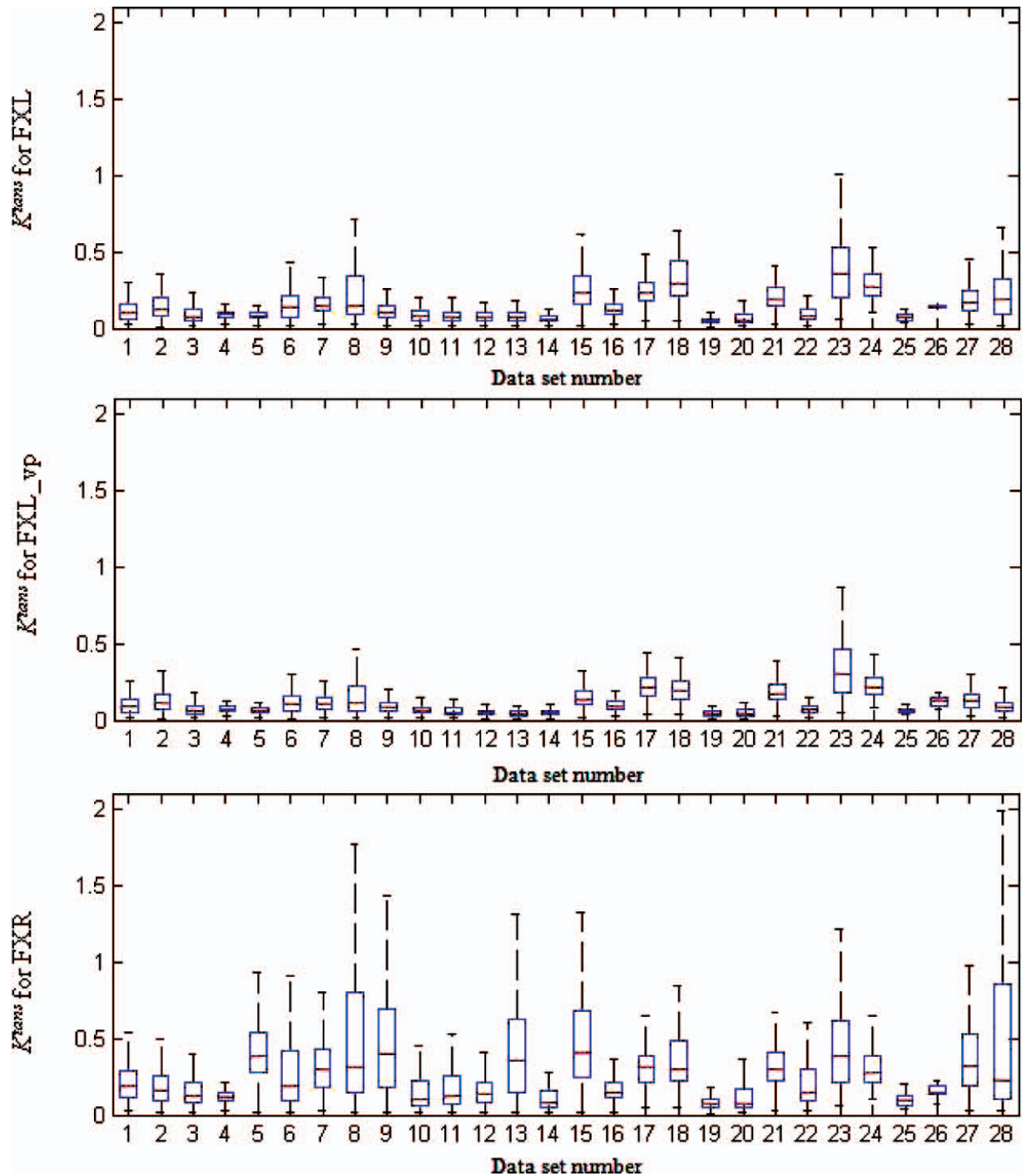


FIG. 4. The box and whisker plots of K^{trans} returned by the FXL, FXL_{vp}, and FXR model, respectively, for all 28 data sets. The outliers are omitted to keep the figure concise. [Color figure can be viewed in the online issue, which is available at wileyonlinelibrary.com.]

values in all data sets and FXL returned the smallest median v_o values in 75% data sets. These results match those reported elsewhere in the literature (24–26).

The percentage of voxels with serial correlation is presented in Fig. 6. The FXL_{vp} and FXR models result in 0.71 and 2.33% voxels with serial correlation respectively, indicating a substantially superior description of the time courses relative to the FXL model, which displayed serial correlation in 17.64% of the voxels. Figure 7 shows the percentage of voxel numbers with small-

est χ^2 , AIC_c , and BIC for each model with 95% confidence intervals. The FXR model displays the smallest χ^2 , AIC_c , and BIC in the majority voxels (47.53, 46.59, and 45.25%, respectively). Note that the 95% confidence intervals of the FXL_{vp} and FXR overlap for χ^2 , AIC_c , and BIC, whereas the 95% confidence intervals of the FXL and the other two models do not overlap.

The average goodness of fit, over all patient sets, is reported in Table 1. The results show that the FXL with v_p model has the smallest mean χ^2 of 4.15×10^{-5} ,

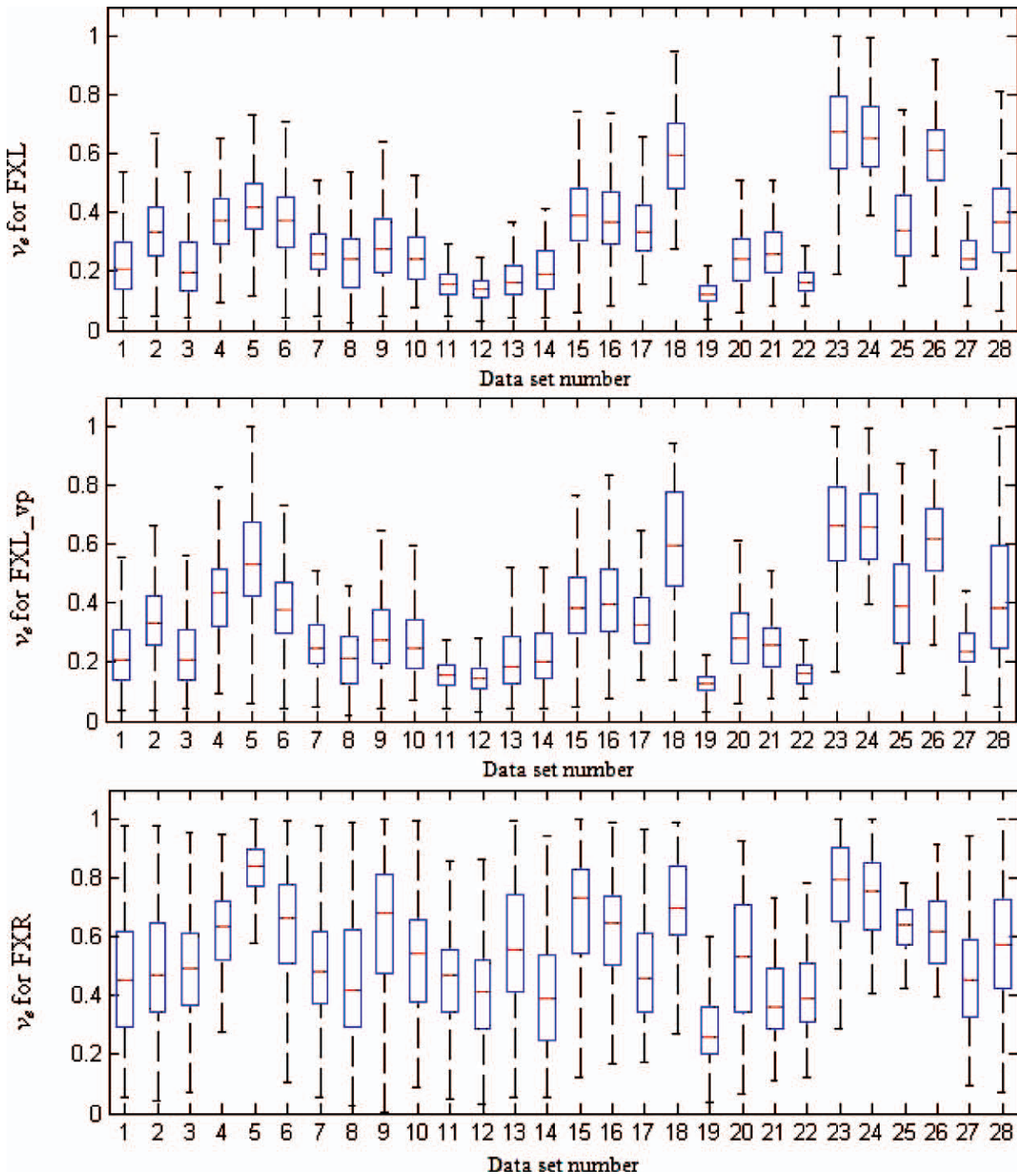


FIG. 5. The box and whisker plots of v_e returned by the FXL, FXL_{vp}, and FXR model, respectively, for all 28 data sets. The outliers are omitted to keep the figure concise. [Color figure can be viewed in the online issue, which is available at wileyonlinelibrary.com.]

whereas the FXR and FXL models have mean χ^2 values of 4.36×10^{-5} and 5.22×10^{-5} , respectively. The average signal-to-noise ratio for the tumor region of interests from the central slice is 14.0 ± 6.5 ; because these are SENSE accelerated scans, the signal-to-noise ratio was computed as the mean of two precontrast scans multiplied by $\sqrt{2}$ and divided by the standard deviation of the difference between those two scans (37). Table 1 also summarizes the other statistical assessment of the three models. The paired *t*-test was applied to each statistical

metric to determine if there was a significant difference between models as quantified by the different statistical measures. The D–W statistic indicated that there was a significant difference ($P < 10^{-6}$) between the FXL and all the other models. The FXL led to the smallest mean D–W value, indicating the FXL model is prone to positive serial correlation. The AIC_c and BIC show that the best balance between goodness of fit and complexity (-263.59 ± 14.69 and -259.93 ± 14.69 , respectively) can be obtained by the FXL_{vp} model. All the *P* values

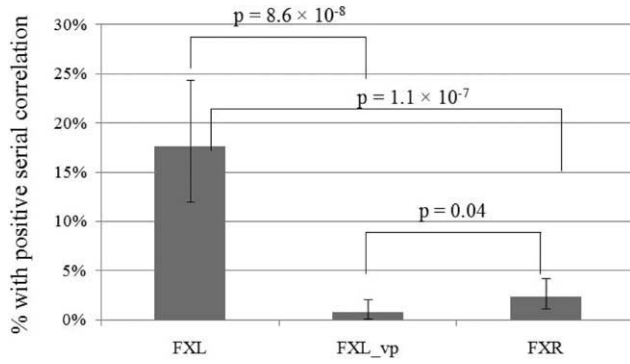


FIG. 6. The percentage of voxel numbers with serial correlation for all tumor voxels is presented. FXL_{vp} and FXR result in 0.71 and 2.33% voxels with serial correlation respectively, indicating substantially superior to FXL which led to 17.64% voxels with serial correlation. The D-W statistic results were significantly different ($P < 10^{-6}$) between the FXL and the other models.

between the FXL and FXL_{vp} and between the FXL and FXR are less than 0.005 in all statistical metrics, whereas there is no significant difference between the FXL_{vp} and FXR models according to the AIC and BIC metrics. These model differences can lead to differences in the actual pharmacokinetic parameter values. The mean parameter values for all tumor voxels of each data set are given in Table 2. Consistent with Figs. 4 and 5, the FXL_{vp} model led to the smallest mean K^{trans} values and the FXR led to the largest mean K^{trans} and mean v_e in all data sets. Furthermore, the P values show significant differences in K^{trans} and v_e values among the three models ($P < 0.005$). The mean v_p returned by the FXL with v_p model is 0.033 ± 0.033 and the mean τ_i returned by the FXR model is 0.37 ± 0.17 s.

The mean CC for all data sets is given in Table 3. The results show that the correlation between K^{trans} returned by the FXL and FXL with v_p models is the strongest (CC = 0.89), whereas the correlation between K^{trans} returned by the FXL with v_p model and the FXR model is the weakest (CC = 0.51). The correlations between v_e returned by different models are similar (from 0.51 to 0.58).

DISCUSSION

The physiological parameters K^{trans} and v_e are measured in practice to both diagnose and assess treatment response in breast cancer (4–9,38), but their values estimated by DCE-MRI analysis are often strongly influenced

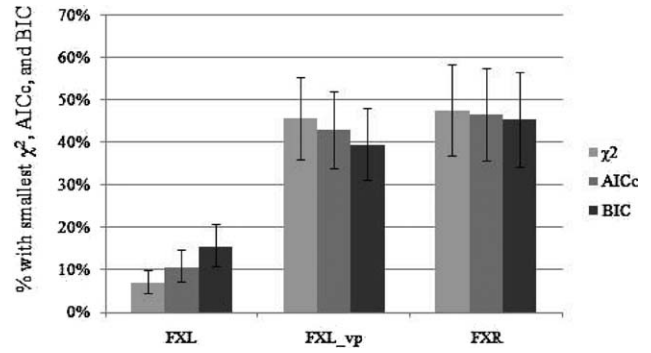


FIG. 7. The percentages of all tumor voxels with the smallest χ^2 , AIC_c, and BIC for each model with 95% confidence intervals are shown. The FXR leads to the majority voxels with smallest statistical measures, indicating the best goodness of fit and balance between the goodness of fit and complexity. See the P values in Table 1.

by which model is selected. We have attempted to offer evidence that the FXL model with a plasma component (Eq. 6) and the FXR model (Eq. 9) are both statistically superior to the FXL model (Eq. 5) in the analysis of human breast cancer DCE time courses. Furthermore, the three models return statistically significantly different K^{trans} and v_e values. Although the FXR model has been argued on physical and physiological grounds (23,24), the question of which model is statistically superior in human breast cancer has not been previously established. Experiments in this study show that the D–W, chi-square, AIC, and BIC all favor the use of either the FXL with the v_p component (FXL_{vp}) or the FXR approach for the patient group used in this study.

Unfortunately, for our data sets, the SXR model was unable to converge on most of the enhancing tumor voxels. One possible reason is that this model calculates both T_{1L} and T_{1S} in Eqs. 7–9, making the fitting procedure more complicated. This severely limited our ability to compare this model to the others. It could be that the limited signal-to-noise ratio available in our breast DCE-MRI acquisitions (where we have tried to balance spatial and temporal resolution requirements) is not sufficient to allow for analysis with this model. Future studies will investigate this point.

A natural extension to the FXR, for which there is physiological motivation, is to add a blood volume component. Unfortunately, adding a blood compartment and still accounting for water exchange between all the

Table 1
Summary of Statistical Measures of Three Models

Data set	D–W			χ^2			AIC _c			BIC		
	FXL	FXL _{vp}	FXR	FXL ($\times 10^{-5}$)	FXL _{vp} ($\times 10^{-5}$)	FXR ($\times 10^{-5}$)	FXL	FXL _{vp}	FXR	FXL	FXL _{vp}	FXR
Mean	1.70	2.04	1.96	5.22	4.15	4.36	–255.96	–263.59	–262.47	–253.52	–259.93	–258.82
Std Dev	0.27	0.24	0.22	2.92	2.85	2.84	13.34	14.69	13.93	13.34	14.69	13.93
	(FXL, FXL _{vp})	(FXL _{vp} , FXR)	(FXL, FXR)	(FXL, FXL _{vp})	(FXL _{vp} , FXR)	(FXL _{vp} , FXR)	(FXL, FXR)	(FXL, FXL _{vp})	(FXL _{vp} , FXR)	(FXL, FXR)	(FXL, FXL _{vp})	(FXL _{vp} , FXR)
P value	8.6×10^{-8}	0.04	1.1×10^{-7}	3.2×10^{-5}	0.015	0.002	6.4×10^{-7}	0.27	0.0005	9.7×10^{-6}	0.27	0.003

Table 2
Summary of Parameter Values Obtained by Three Models

Data sets	K^{trans} (min^{-1})			v_e			v_p	τ_i (s)
	FXL	FXL_ v_p	FXR	FXL	FXL_ v_p	FXR	FXL_ v_p	FXR
Mean	0.16	0.12	0.35	0.33	0.35	0.55	0.033	0.37
Std Dev	0.10	0.07	0.22	0.15	0.15	0.12	0.033	0.17
<i>P</i> value	(FXL, FXL_ v_p) 5.4×10^{-6}	(FXL_ v_p , FXR) 3.2×10^{-6}	(FXL, FXR) 2.7×10^{-5}	(FXL, FXL_ v_p) 0.002	(FXL_ v_p , FXR) 7.5×10^{-14}	(FXL, FXR) 0.002	N/A	N/A

relevant compartments (intravascular, extravascular-extracellular, and extravascular-intracellular) yields a model that is currently difficult to use in practical situations. More specifically, adding a vascular term to Eq. 9 and still accounting for the effects of water exchange requires a three-site (rather than just two sites) model which has (at least) five free parameters (39) and is currently unsuitable for voxel level analysis. Indeed, this model has been studied in simulations (39); and perhaps more extensive studies are required to determine which combinations of parameters can be reliably assessed with a given model. Adding a vascular term to FXL (Eq. 6) is straightforward and several investigators have done so and applied this model (see, e.g., Refs. 40–42) in vivo. Li et al. (39) have recently shown that when there is sufficient CA extravasation from plasma to interstitium, such as in some tumors, exclusion of a plasma term is an acceptable assumption. But, when contrast extravasation is minimal, such as when $K^{trans} < 0.01 \text{ min}^{-1}$, exclusion of the plasma term may cause significant errors.

As reported in Table 2, the FXR model results in higher mean K^{trans} and v_e (0.35 min^{-1} and 0.55 , respectively), whereas the FXL and FXL_ v_p lead to the mean K^{trans} of 0.16 and 0.12 min^{-1} and v_e of 0.33 and 0.35 , respectively. The results are reasonable, though a bit elevated, compared with other studies (43–45). For instance, the work of Li et al. (43) reported that the mean K^{trans} and v_e (obtained from a FXL analysis) at baseline in breast cancer were 0.33 min^{-1} and 0.44 , respectively. In the effort of Li et al. (44), the mean K^{trans} and v_e (obtained from the FXR model) were $\sim 0.15 \text{ min}^{-1}$ and 0.6 , respectively, for breast cancer. Moreover, the maximum v_e reported in Ref. 44 was up to 0.8 . The study of Miller et al. (45) also showed that the median K^{trans} of baseline for the patients with metastatic breast cancer ranged from 0.65 to 1.7 min^{-1} . One possible reason for the higher values in K^{trans} and v_e is the limitation of the models for tumors with the extreme spatial heterogeneity. For example, in regions that are poorly perfused the CA will accumulate and wash out slowly, which can lead to large values in v_e . For example, Jansen et al. (46)

found that the CA could accumulate within the milk ducts filled with ductal carcinoma in situ. Under this situation, the models investigated in this study will not be able to accurately estimate the extravascular-extracellular volume. Another source of possible error could be in the measured AIF. The inaccuracy in the AIF could cause the propagation of errors in the estimated parameters. The temporal resolution of 16 s used in this study is not optimal for AIF characterization (although it is reasonable as it represents a compromise between high temporal resolution and large spatial coverage), and it may miss the peak of AIF and therefore cause larger values of parameters, particularly K^{trans} . Also, direct measurements from the artery are likely to underestimate the peak amplitude of the AIF due to T_2^* and exchange effects. Those factors affect the accuracy of the AIF, and consequently, affect the measurements of the pharmacokinetic parameters.

Use of the FXL with a plasma fraction and the FXR model resulted in a substantial reduction in percentage of voxels showing positive serial correlation of residuals: 17.64 , 0.71 , and 2.33% for the FXL, FXL_ v_p , and FXR models, respectively. In 47.53% of voxels, the χ^2 indicated that the FXR model was superior, and in 46.59 and 45.25% of voxels, the AIC_c and BIC also indicated that the FXR model was superior. This translated into significant differences in the values of K^{trans} and v_e that were extracted in the voxel-by-voxel analyses, and underscores the fact that different models can yield different pharmacokinetic parameter values. It is therefore of great importance to select the appropriate model to analyze the DCE-MRI time courses so that the most accurate parameter estimates are obtained. It is plausible that inappropriate model selection can lead to inaccuracy in, for example, predicting treatment response. It was the overall goal of this study to provide a reasonable rationale for model selection. Although the results presented do not provide a physical or physiological basis for selecting a particular model, they do provide an objective statistical basis for selecting a particular model. In general, the applicability of each model, as well as other

Table 3
The CC Between K^{trans} and v_e Obtained by Three Models

Data sets	CC of K^{trans}			CC of v_e		
	(FXL, FXL_ v_p)	(FXL_ v_p , FXR)	(FXL, FXR)	(FXL, FXL_ v_p)	(FXL_ v_p , FXR)	(FXL, FXR)
Mean	0.89	0.51	0.72	0.58	0.51	0.58
Std Dev	0.13	0.24	0.17	0.11	0.16	0.12

models, will depend on the physiology, anatomy, and heterogeneity of the cancer and surrounding tissues. The patients selected in this study have clinical stage II/III invasive mammary carcinoma and are at sufficient risk of recurrence based on pretreatment clinical parameters of size, grade, age, and nodal status. For this group of patients, the FXL v_p and FXR models show significant advantages. However, early noninvasive cancers (e.g., ductal carcinoma in situ) may have less blood volume (lower v_p values) compared to the locally advanced breast cancer. Cell size and tumor heterogeneity also have an influence on parameters estimated by different models. It is difficult to know, a priori, the underlying physiological characteristics of a given voxel of breast tissue, so it is difficult to select which model is most realistic. In this case, a statistical assessment of model fitting is not only a reasonable way to proceed but also practical because it provides a rigorous reason for selecting a given model over another. Furthermore, the statistical results can reflect some of the underlying physiological properties of a given breast tumor. For example, in cases where the FXL v_p model is selected by the statistical measures as the most accurate, we can infer that those voxels have a significant plasma component (i.e., $v_p > \sim 0.03$), whereas in those situations where the FXR model is selected, we can infer that the difference in concentration of CA between the extravascular-extracellular space and the extravascular-intracellular space must be great enough to drive the system out of the FXL.

The ultimate test for these models is their ability to answer important clinical questions, such as treatment effects during longitudinal studies of patients undergoing neoadjuvant chemotherapy or the ability to distinguish malignant breast tumors from benign lesions. Li et al. (29) have performed preliminary analyses on benign and malignant breast diseases. We have an ongoing study testing the abilities of parameters returned by different models to predict the response of breast tumors to neoadjuvant chemotherapy (47).

In conclusion, the results of the four statistical metrics used in this study indicate that, for the group of patients selected for this study, the FXL with a plasma component and the FXR model have significant advantages over the FXL and SXR models. The methods outlined here also provide a statistical mechanism for selecting and assessing other DCE models. Moreover, our results highlight the possibility that in heterogeneous tissues, the most appropriate models may vary between voxels.

ACKNOWLEDGMENTS

The authors thank Ms. Donna Butler, Ms. Robin Avison, and Ms. Wanda Smith for expert technical assistance and John Huff, M.D., for many informative discussions.

REFERENCES

- Choyke PL, Dwyer AJ, Knopp MV. Functional tumor imaging with dynamic contrast-enhanced magnetic resonance imaging. *J Magn Reson Imaging* 2003;17 (5):509–520.
- Padhani AR, Leach MO. Antivascular cancer treatments: functional assessments by dynamic contrast-enhanced magnetic resonance imaging. *Abdom Imaging* 2005;30 (3):324–341.
- Yankeelov TE, Gore JC. Dynamic contrast enhanced magnetic resonance imaging in oncology: theory, data acquisition, analysis, and examples. *Curr Med Imaging Rev* 2007;3 (2):91–107.
- Kuhl CK, Schrading S, Leutner CC, Morakkabati-Spitz N, Wardelmann E, Fimmers R, Kuhn W, Schild HH. Mammography, breast ultrasound, and magnetic resonance imaging for surveillance of women at high familial risk for breast cancer. *J Clin Oncol* 2005;23 (33):8469–8476.
- Leach MO, Boggis CR, Dixon AK, Easton DF, Eeles RA, Evans DG, Gilbert FJ, Griebbsch I, Hoff RJ, Kessar P, Lakhani SR, Moss SM, Nerurkar A, Padhani AR, Pointon LJ, Thompson D, Warren RM. Screening with magnetic resonance imaging and mammography of a UK population at high familial risk of breast cancer: a prospective multicentre cohort study (MARIBS). *Lancet* 2005;365 (9473):1769–1778.
- Lehman CD, Blume JD, Weatherall P, Thickman D, Hylton N, Warner E, Pisano E, Schnitt SJ, Gatsonis C, Schnall M, DeAngelis GA, Stomper P, Rosen EL, O'Loughlin M, Harms S, Bluemke DA. Screening women at high risk for breast cancer with mammography and magnetic resonance imaging. *Cancer* 2005;103 (9):1898–1905.
- Sardanelli F, Podo F, D'Agnolo G, Verdecchia A, Santaquilani M, Musumeci R, Trecate G, Manoukian S, Morassut S, de Giacomi C, Federico M, Cortesi L, Corcione S, Cirillo S, Marra V, Cilotti A, Di Maggio C, Fausto A, Preda L, Zuiani C, Contegiacomo A, Orlacchio A, Calabrese M, Bonomo L, Di Cesare E, Tonutti M, Panizza P, Del Maschio A. Multicenter comparative multimodality surveillance of women at genetic-familial high risk for breast cancer (HIBCRIT study): interim results. *Radiology* 2007;242 (3):698–715.
- Warner E, Plewes DB, Hill KA, Causer PA, Zubovits JT, Jong RA, Cutrara MR, DeBoer G, Yaffe MJ, Messner SJ, Meschino WS, Piron CA, Narod SA. Surveillance of BRCA1 and BRCA2 mutation carriers with magnetic resonance imaging, ultrasound, mammography, and clinical breast examination. *JAMA* 2004;292 (11):1317–1325.
- Lord SJ, Lei W, Craft P, Cawson JN, Morris I, Walleser S, Griffiths A, Parker S, Houssami N. A systematic review of the effectiveness of magnetic resonance imaging (MRI) as an addition to mammography and ultrasound in screening young women at high risk of breast cancer. *Eur J Cancer* 2007;43 (13):1905–1917.
- Cheung YC, Chen SC, Su MY, See LC, Hsueh S, Chang HK, Lin YC, Tsai CS. Monitoring the size and response of locally advanced breast cancers to neoadjuvant chemotherapy (weekly paclitaxel and epirubicin) with serial enhanced MRI. *Breast Cancer Res Treat* 2003;78 (1):51–58.
- Chou CP, Wu MT, Chang HT, Lo YS, Pan HB, Degani H, Furman-Haran E. Monitoring breast cancer response to neoadjuvant systemic chemotherapy using parametric contrast-enhanced MRI: a pilot study. *Acad Radiol* 2007;14 (5):561–573.
- Delille JP, Slanetz PJ, Yeh ED, Halpern EF, Kopans DB, Garrido L. Invasive ductal breast carcinoma response to neoadjuvant chemotherapy: noninvasive monitoring with functional MR imaging pilot study. *Radiology* 2003;228 (1):63–69.
- Martincich L, Montemurro F, De Rosa G, Marra V, Ponzzone R, Cirillo S, Gatti M, Biglia N, Sarotto I, Sismondi P, Regge D, Aglietta M. Monitoring response to primary chemotherapy in breast cancer using dynamic contrast-enhanced magnetic resonance imaging. *Breast Cancer Res Treat* 2004;83 (1):67–76.
- Padhani AR, Hayes C, Assersohn L, Powles T, Makris A, Suckling J, Leach MO, Husband JE. Prediction of clinicopathologic response of breast cancer to primary chemotherapy at contrast-enhanced MR imaging: initial clinical results. *Radiology* 2006;239 (2):361–374.
- Pickles MD, Lowry M, Manton DJ, Gibbs P, Turnbull LW. Role of dynamic contrast enhanced MRI in monitoring early response of locally advanced breast cancer to neoadjuvant chemotherapy. *Breast Cancer Res Treat* 2005;91 (1):1–10.
- Nagashima T, Sakakibara M, Nakamura R, Arai M, Kadowaki M, Kazama T, Nakatani Y, Koda K, Miyazaki M. Dynamic enhanced MRI predicts chemosensitivity in breast cancer patients. *Eur J Radiol* 2006;60 (2):270–274.
- Chang YC, Huang CS, Liu YJ, Chen JH, Lu YS, Tseng WY. Angiogenic response of locally advanced breast cancer to neoadjuvant chemotherapy evaluated with parametric histogram from dynamic contrast-enhanced MRI. *Phys Med Biol* 2004;49 (16):3593–3602.
- Rieber A, Brambs HJ, Gabelmann A, Heilmann V, Kreienberg R, Kuhn T. Breast MRI for monitoring response of primary breast cancer to neo-adjuvant chemotherapy. *Eur Radiol* 2002;12 (7):1711–1719.
- Schott AF, Roubidoux MA, Helvie MA, Hayes DF, Kleer CG, Newman LA, Pierce LJ, Griffith KA, Murray S, Hunt KA, Paramagul C,

- Baker LH. Clinical and radiologic assessments to predict breast cancer pathologic complete response to neoadjuvant chemotherapy. *Breast Cancer Res Treat* 2005;92 (3):231–238.
20. Landis CS, Li X, Telang FW, Molina PE, Palyka I, Vetek G, Springer CS Jr. Equilibrium transcytolemmal water-exchange kinetics in skeletal muscle in vivo. *Magn Reson Med* 1999;42 (3):467–478.
 21. Yu HJ, Chen JH, Mehta RS, Nalcioglu O, Su MY. MRI measurements of tumor size and pharmacokinetic parameters as early predictors of response in breast cancer patients undergoing neoadjuvant anthracycline chemotherapy. *J Magn Reson Imaging* 2007;26 (3):615–623.
 22. Ah-See ML, Makris A, Taylor NJ, Harrison M, Richman PI, Burcombe RJ, Stirling JJ, d'Arcy JA, Collins DJ, Pittam MR, Ravichandran D, Padhani AR. Early changes in functional dynamic magnetic resonance imaging predict for pathologic response to neoadjuvant chemotherapy in primary breast cancer. *Clin Cancer Res* 2008;14 (20):6580–6589.
 23. Landis CS, Li X, Telang FW, Coderre JA, Micca PL, Rooney WD, Latour LL, Vetek G, Palyka I, Springer CS. Determination of the MRI contrast agent concentration time course in vivo following bolus injection: effect of equilibrium transcytolemmal water exchange. *Magn Reson Med* 2000;44 (4):563–574.
 24. Yankeelov TE, Rooney WD, Li X, Springer CS. Variation of the relaxographic “shutter-speed” for transcytolemmal water exchange affects the CR bolus-tracking curve shape. *Magn Reson Med* 2003; 50 (6):1151–1169.
 25. Zhou R, Pickup S, Yankeelov TE, Springer CS Jr, Glickson JD. Simultaneous measurement of arterial input function and tumor pharmacokinetics in mice by dynamic contrast enhanced imaging: effects of transcytolemmal water exchange. *Magn Reson Med* 2004;52 (2):248–257.
 26. Kim S, Quon H, Loevner LA, Rosen MA, Dougherty L, Kilger AM, Glickson JD, Poptani H. Transcytolemmal water exchange in pharmacokinetic analysis of dynamic contrast-enhanced MRI data in squamous cell carcinoma of the head and neck. *J Magn Reson Imaging* 2007;26 (6):1607–1617.
 27. Huang W, Li X, Morris EA, Tudorica A, Venkatraman ES, Wang Y, Xu J. Shutter-speed DCE-MRO pharmacokinetic analyses facilitate the discrimination of malignant and benign breast disease. *Proc Intl Soc Magn Reson Med* 2007;15:141.
 28. Yankeelov TE, Rooney WD, Huang W, Dyke JP, Li X, Tudorica A, Lee JH, Koutcher JA, Springer CS Jr. Evidence for shutter-speed variation in CR bolus-tracking studies of human pathology. *NMR Biomed* 2005;18 (3):173–185.
 29. Li X, Huang W, Yankeelov TE, Tudorica A, Rooney WD, Springer CS Jr. Shutter-speed analysis of contrast reagent bolus-tracking data: preliminary observations in benign and malignant breast disease. *Magn Reson Med* 2005;53 (3):724–729.
 30. Donaldson SB, West CM, Davidson SE, Carrington BM, Hutchison G, Jones AP, Sourbron SP, Buckley DL. A comparison of tracer kinetic models for T_1 -weighted dynamic contrast-enhanced MRI: application in carcinoma of the cervix. *Magn Reson Med* 2010;63 (3):691–700.
 31. Lowry M, Zelhof B, Liney GP, Gibbs P, Pickles MD, Turnbull LW. Analysis of prostate DCE-MRI: comparison of fast exchange limit and fast exchange regimen pharmacokinetic models in the discrimination of malignant from normal tissue. *Invest Radiol* 2009;44 (9):577–584.
 32. Yankeelov TE, Lepage M, Chakravarthy A, Broome EE, Niermann KJ, Kelley MC, Meszoely I, Mayer IA, Herman CR, McManus K, Price RR, Gore JC. Integration of quantitative DCE-MRI and ADC mapping to monitor treatment response in human breast cancer: initial results. *Magn Reson Imaging* 2007;25 (1):1–13.
 33. Kety SS. The theory and applications of the exchange of inert gas at the lungs and tissues. *Pharmacol Rev* 1951;3 (1):1–41.
 34. Li X, Welch EB, Arlinghaus LR, Chakravarthy AB, Xu L, Farley J, Lovelless ME, Mayer I, Kelley M, Meszoely I, Means-powell J, Abramson V, Grau A, Gore JC, Yankeelov TE. A novel AIF tracking method and a comparison of DCE-MRI parameters using individual and population-based AIFs in human breast cancer. *Phys Med Biol* 2011;56:5753–5769.
 35. Draper NR, Smith H. *Applied regression analysis*. New York: John Wiley & Sons; 1998.
 36. Akaike H. A new look at the statistical model identification. *IEEE Trans Auto Control* 1974 (19):716–723.
 37. Dietrich O, Raya JG, Reeder SB, Reiser MF, Schoenberg SO. Measurement of signal-to-noise ratios in MR images: influence of multichannel coils, parallel imaging, and reconstruction filters. *J Magn Reson Imaging* 2007;26 (2):375–385.
 38. Morris EA. Diagnostic breast MR imaging: current status and future directions. *Radiol Clin North Am* 2007;45 (5):863–880, vii.
 39. Li X, Rooney WD, Springer CS Jr. A unified magnetic resonance imaging pharmacokinetic theory: intravascular and extracellular contrast reagents. *Magn Reson Med* 2005;54 (6):1351–1359.
 40. Wilmes LJ, Pallavicini MG, Fleming LM, Gibbs J, Wang D, Li KL, Partridge SC, Henry RG, Shalinsky DR, Hu-Lowe D, Park JW, McShane TM, Lu Y, Brasch RC, Hylton NM. AG-013736, a novel inhibitor of VEGF receptor tyrosine kinases, inhibits breast cancer growth and decreases vascular permeability as detected by dynamic contrast-enhanced magnetic resonance imaging. *Magn Reson Imaging* 2007;25 (3):319–327.
 41. Fournier LS, Novikov V, Lucidi V, Fu Y, Miller T, Floyd E, Shames DM, Brasch RC. MR monitoring of cyclooxygenase-2 inhibition of angiogenesis in a human breast cancer model in rats. *Radiology* 2007;243 (1):105–111.
 42. Rydland J, BjOrnerud A, Haugen O, Torheim G, Torres C, Kvistad KA, Haraldseth O. New intravascular contrast agent applied to dynamic contrast enhanced MR imaging of human breast cancer. *Acta Radiol* 2003;44 (3):275–283.
 43. Li S, Taylor N, Mehta S, Hughes N, Stirling JJ, Simcock I, Collins DJ, d'Arcy JA, Leach MO, Harris A, Makris A, Padhani AR. Evaluating the early effects of anti-angiogenic treatment in human breast cancer with intrinsic susceptibility-weighted and diffusion-weighted MRI: initial observations. *Proc Intl Soc Magn Reson Med* 2011;19:342.
 44. Li X, Huang W, Morris EA, Tudorica LA, Seshan VE, Rooney WD, Tagge I, Wang Y, Xu J, Springer CS Jr. Dynamic NMR effects in breast cancer dynamic-contrast-enhanced MRI. *Proc Natl Acad Sci USA* 2008;105 (46):17937–17942.
 45. Miller KD, Trigo JM, Wheeler C, Barge A, Rowbottom J, Sledge G, Baselga J. A multicenter phase II trial of ZD6474, a vascular endothelial growth factor receptor-2 and epidermal growth factor receptor tyrosine kinase inhibitor, in patients with previously treated metastatic breast cancer. *Clin Cancer Res* 2005;11 (9):3369–3376.
 46. Jansen SA, Paunesku T, Fan X, Woloschak GE, Vogt S, Conzen SD, Krausz T, Newstead GM, Karczmar GS. Ductal carcinoma in situ: X-ray fluorescence microscopy and dynamic contrast-enhanced MR imaging reveals gadolinium uptake within neoplastic mammary ducts in a murine model. *Radiology* 2009;253 (2):399–406.
 47. Li X, Arlinghaus LR, Welch EB, Chakravarthy AB, Xu L, Farley J, Mayer I, Kelley M, Meszoely I, Means-Powell J, Abramson V, Grau A, Levy M, Gore JC, Yankeelov TE. Early DCE-MRI changes predict residual enhancing volume in breast cancer patients undergoing neoadjuvant chemotherapy. *Proc Intl Soc Magn Reson Med* 2011;19:1025.